

Stability and lifetime of diffusion-trapped oxygen in oxide-derived copper CO₂ reduction electrocatalysts

Received: 29 March 2023

Zan Lian¹✉, Federico Dattila² & Núria López¹✉

Accepted: 23 February 2024

Published online: 01 April 2024

Check for updates

Oxide-derived Cu has an excellent ability to promote C–C coupling in the electrochemical carbon dioxide reduction reaction. However, these materials largely rearrange under reaction conditions; therefore, the nature of the active site remains controversial. Here we study the reduction process of oxide-derived Cu via large-scale molecular dynamics with a precise neural network potential trained on first-principles data and introducing experimental conditions. The oxygen concentration in the most stable oxide-derived Cu increases with an increase of the pH, potential or specific surface area. In long electrochemical experiments, the catalyst would be fully reduced to Cu, but removing all the trapped oxygen takes a considerable amount of time. Although the highly reconstructed Cu surface provides various sites to adsorb oxygen more strongly, the surface oxygen atoms are not stable under common experimental conditions. This work provides insight into the evolution of oxide-derived Cu catalysts and residual oxygen during reaction and also a deep understanding of the nature of active sites.

Closing the carbon cycle through electrochemical carbon dioxide (CO₂) reduction with renewable energy has drawn attention for its potential to create net-zero technologies^{1–3}. Cu-based catalysts are considered the only class of materials able to perform C–C coupling^{4,5} and to provide valuable C₂₊ products at high reaction rates^{6–11}. Cu and particularly oxide-derived Cu (OD-Cu) catalysts exhibit significant structure sensitivity^{12–15}; the latter produce C₂₊ with higher current density and faradaic efficiency (FE = 45% to 80%) at reasonable overpotentials ($U = -0.40$ to -1.00 V versus the reversible hydrogen electrode (V_{RHE}))^{12,16–20}. These materials show a highly dynamic behaviour with profound stoichiometric and structural rearrangements under the experimental conditions^{21–24}.

The unique performance of OD-Cu has been attributed to the singularities of its morphology^{23–28}; however, the real structure under reaction conditions remains controversial^{15,16,29–36} due to its highly dynamic behaviour under experimental conditions. According to X-ray diffraction and Raman experiments^{31,37}, OD-Cu should be reduced in

the bulk, which is also consistent with the thermodynamics^{38,39}, but pulse experiments¹⁶ show that residual oxygen^{40,41} can be trapped, thus enhancing the electrocatalytic process^{42,43}. Uniformly dispersed oxide nanoparticles NPs reduced under CO₂ reduction reaction (CO₂RR) conditions were found to evolve morphologically very rapidly via an electrochemical scrambling process, with an initial formation of Cu aggregates that under air exposure change into Cu₂O nanocubes⁶. Moreover, the existence of oxygen species under reductive conditions was investigated with grazing incidence hard X-ray photoelectron spectroscopy of OD-Cu prepared by the reduction of Cu oxide with H₂ without exposure to air. These conditions enabled authors to extract the oxygen depth distribution profiles²⁹. These experiments identify separated Cu₂O buried in the material; oxygen in the lattice close to the surface, replacing Cu atomic positions; and O as interstitials in the Cu. Computational models have attempted to disentangle such complexity, but they face similar severe limitations. Models for fully oxygen-depleted materials have been investigated in

¹Institute of Chemical Research of Catalonia (ICIQ-CERCA), The Barcelona Institute of Science and Technology (BIST), Tarragona, Spain. ²Department of Applied Science and Technology (DISAT), Politecnico di Torino, Turin, Italy. ✉e-mail: zlian@icicq.es; nlopez@icicq.es

classical molecular dynamics (MD)⁴⁴. Particularly, four types of sites were reported for roughened copper surfaces consisting of 10^6 – 10^7 atoms created by removing heteroatoms from cuprous oxide, nitride, phosphide and sulfide⁴⁴ with classical effective medium theory. The results show that over-coordinated four-fold hollow sites were beneficial to produce C_{2+} species in the electrochemical CO_2 RR. Alternatively, OD-Cu models were investigated by ab initio MD (AIMD)¹⁴ but at fixed oxygen contents, that is, decoupled from the experimental conditions.

Recent developments in neural network potential (NNP) derived from massive density functional theory (DFT) simulations hold the key for a proper structural and energetic analysis of the long-time and extended length OD-Cu dynamic phenomena. A first attempt that shows the feasibility of the approach⁴⁵ was carried out for an OD-Cu slab built by removing surface oxygens gradually until no oxygen appears on the surface after 1 ns equilibration. A pure Cu surface with a base of Cu_2O was finally formed, and the results show that the Cu-only planar-square and convex-square sites are selective to ethylene. However, oxygen diffusion is difficult to observe due to the short times and low temperatures in typical MD simulations; thus, the process of Cu_2O reduction to Cu observed in many experiments has not been considered in these state-of-the-art simulations.

Both the content and the depth profile of the oxygen distribution are highly contentious since OD-Cu is easily re-oxidized when it is characterized by ex situ methods, limiting the experimental capability to assess active and selective ensembles during operation. To gain an insight into the change of OD-Cu structures during the electrochemical CO_2 RR, here we trained an accurate NNP to address the highly dynamic nature of the catalysts, strongly coupled to the history of the sample and to the reaction conditions, and we analyse the kinetics of oxygen diffusion in detail and compare it to the most recent experimental observations. Based on the simulations, the OD-Cu structures under different conditions and distributions of active sites were obtained, thus paving the way for their control.

Results

Methodological approach

The modelling procedure fits a NNP to simulate OD-Cu systems, in order to perform long MD simulations coupled to an external oxygen reservoir, to identify the most likely oxygen contents under different experimental conditions (Fig. 1). To this end, we generated a DFT (Perdew–Burke–Ernzerhof functional and refitted DFT-D2 van der Waals parameters (PBE-D2; (refs. 46–49)) initial dataset with the most common Cu, Cu_xO and Cu_2O models, generated by optimization and AIMD simulations of the bulk and surface structures.

The Behler–Parrinello high-dimensional NNP (HDNNP)⁵⁰ was constructed using a neural network potential package (n2p2)⁵¹ on the initial dataset (Fig. 1), as described in the Methods. The NNPs were trained via multistream extended Kalman filter algorithms using energies and forces, and the dataset was expanded via active learning (Fig. 1). In short, two NNPs were trained with the initial dataset. Some 1–25% of structures of the dataset were used to perform the neural-network-based MD (NN-MD) simulations using one of the NNPs. The NN-MD simulations were performed using Large-scale Atomic/Molecular Massively Parallel Simulator (LAMMPS)⁵² code with the NNP interface from n2p2 (ref. 53). We collected 1/1000 of total structures obtained from the NN-MD as the seeds for further DFT simulations. These were further selected as follows: one third of structures whose symmetry function values are not within the range of the current dataset (that is, extrapolations⁵⁴) and by comparison of the two NNP runs, when the differences between two predictions (energy and forces) are larger than a threshold (-5 – $10 \times$ root mean squared error (r.m.s.e.)). The latter strategy allows the identification of structures beyond the explored structure space as an interpolation. Then the dataset was updated with the DFT values for these newly calculated structures. Finally, to ensure the robustness of the potential⁵⁵, *NVT* simulations

for models under extreme conditions (at least 1,200 K, for 1 ns) were performed (Supplementary Note 1 and Supplementary Figs. 1–3). These models include the following: a Cu slab with 3,240 atoms generated by removing all oxygens from a Cu_2O (111) pristine system; for Cu_2O , a $Cu_{1415}O_{784}$ cluster; and for Cu_xO , a slab of OD-Cu ($Cu_{444}O_{56}$) from our previous study¹⁴.

To ensure representativity and transferability, the dataset was constructed in two stages. First, the datasets for Cu and Cu_2O were built separately via active learning. Then the intermediate composition structures of Cu_xO were selected. In total, 433 iterations of the active learning process were conducted, in which 8.16×10^{10} steps were run from NN-MDs; 8.30×10^7 structures were compared using two NNPs; and a final dataset with 59,491 points was obtained (Supplementary Table 1). The NNPs applied in the following MD simulation were trained using the final dataset. From the model, the r.m.s.e. of the energy is 4.58 meV per atom and the r.m.s.e. of force is $63.61 \text{ meV } \text{Å}^{-1}$ on the training set, and 4.59 meV per atom and $63.48 \text{ meV } \text{Å}^{-1}$ on the test set, as shown in Supplementary Fig. 4. The energy errors are one order of magnitude smaller than the requirement for chemical accuracy (1 kcal mol^{-1} , that is, 43 meV per atom), which denotes that the NNP has reached the same level of chemical accuracy as the reference PBE-D2 functional. Similar errors in the training and test sets indicate no overfitting.

Thermodynamics of the OD-Cu reduction

To address the fraction of oxygen in OD-Cu under different conditions from a thermodynamic point of view, we started with a perfect Cu_2O (111) slab to examine the role of pH, electric potential and specific surface area (SSA; surface/volume; Fig. 2). Electric potential and pH were introduced through the computational hydrogen electrode⁵⁶. The O-deficient configurations were simulated by the sequential removal of O atoms. For each step, the same number of oxygens (1/48 of the total number of oxygens in the perfect slab) were randomly chosen and removed from the previous structure until all oxygen atoms were removed after 48 steps. Ten random runs were completed to achieve statistical significance. The thermodynamic minima were identified for each case by using a NN-MD annealing simulation (Supplementary Note 2).

Figure 2a shows the energy of OD-Cu reduction as a function of pH. At low pH, OD-Cu tends to be fully reduced to generate pure copper. However, at high pH values, which are typical of highly active and ethylene-selective CO_2 RR electrolyzers⁵⁷, all the steps of the reduction are endothermic, and the perfect Cu_2O is the most stable state. At intermediate pH, the partially reduced Cu_2O system is the thermodynamic ground state. In electrochemical media, with $KHCO_3$ buffer as the electrolyte (pH 6.8–8), about 8.6 at.% oxygen would remain in a system with a SSA of 0.070 Å^{-1} (diameter of 8.6 nm; Supplementary Table 2) at zero potential versus the standard hydrogen electrode (SHE). However, the elimination of the first 37.5% (18/48) of the oxygens is endothermic, which indicates that starting the reduction will require a driving force. As expected, the driving force can be the electric potential, as shown in Fig. 2b; at more reductive potentials, the reduction to copper is favourable. Metallic copper is more favourable than all the partially reduced OD-Cu structures at computational potentials as small as -0.19 V versus the SHE ($V_{SHE} + 0.29 V_{RHE}$). As an approximation to kinetics, we considered the step with the largest positive reaction energy as the potential limiting step that prevents further reduction. This results in a computational potential of $-0.39 V_{SHE}$ ($+0.09 V_{RHE}$) to ensure that all steps are exothermic, indicating that OD-Cu reduction is kinetically limited at weak reduction potentials. The potential for the limiting step was obtained from the mean energy diagram of the ten random reduction simulations. For the single-energy diagrams, the average potential is $-1.09 V_{SHE}$ with a sample standard deviation of 0.36 V, indicating the variance resulting from the annealing simulations and the differently chosen removal order of oxygen.

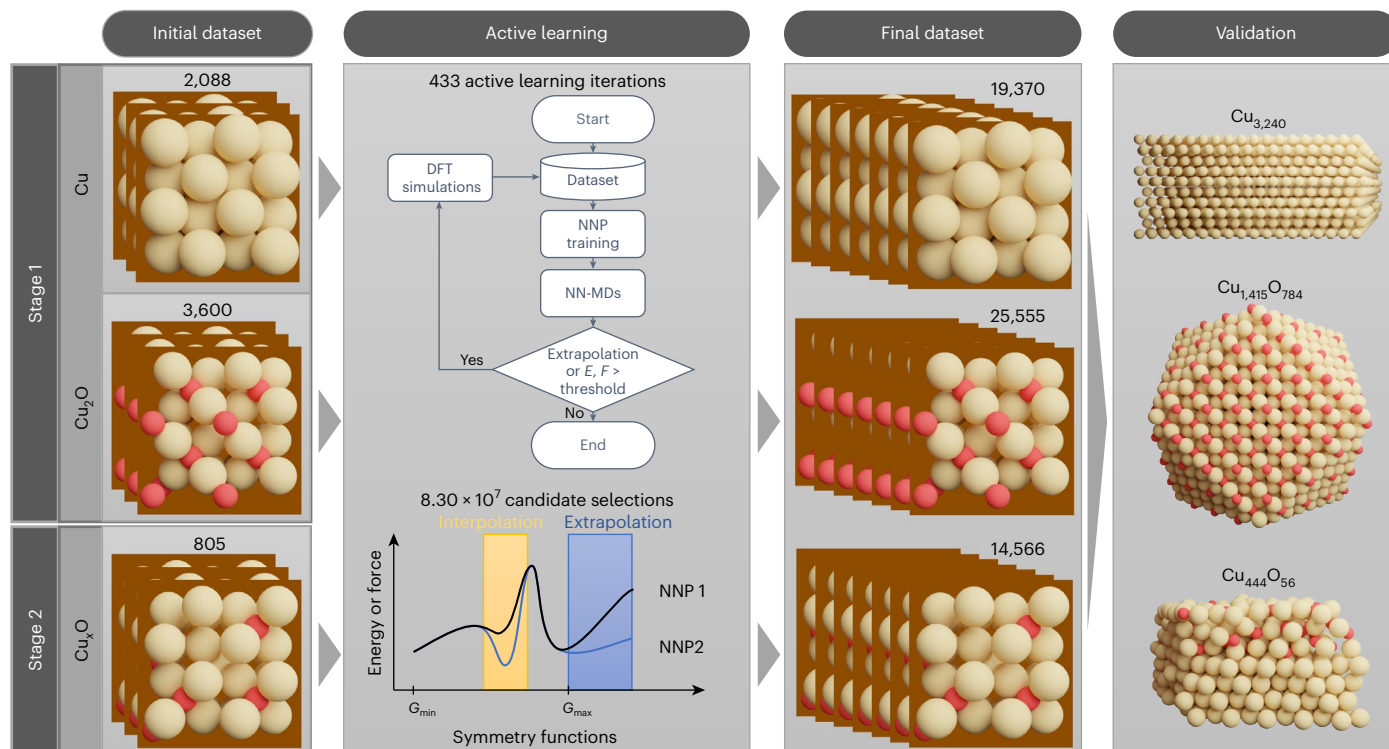


Fig. 1 | Computational modelling approach for constructing the NNP. The data were collected in two stages. In stage 1, the structures of Cu and Cu₂O were selected via the active learning procedure. In stage 2, the dataset of Cu_xO was built based on the dataset of stage 1. In the active learning process, 433 iterations were performed in total, 8.16×10^{10} steps were run from NN-MDs and 8.30×10^7 structures were checked for extrapolation and interpolation. In the end, the final

dataset consists of 59,491 points containing 1,801,491 atomic environments, and the NNPs apply to all three validation structures, which were run for 1 ns without any extrapolation at at least 1,200 K (Supplementary Note 1). *E*, energy; *F*, force; *G*_{min}, minimum of explored symmetric function space; and *G*_{max}, maximum of explored symmetric function space.

To understand the size effect on the reduction degree of OD-Cu, slabs of different thicknesses (equivalent to spherical nanoparticles of diameters between 17.5 and 4.1 nm in the SSA) were simulated. Figure 2c shows that the final state differs significantly and approaches the value of the bulk phase as the SSA decreases. Larger nanoparticles (lower SSA) keep lower oxygen quantities, while the smallest one retains 16.5 at.% of O atoms, and the overall reaction energy of the latter is slightly endothermic (Supplementary Table 2). In general, the lower the SSA, the larger the amount of energy per Cu₂O_x released to reach the same reduction level. On the contrary, the higher the SSA, the more oxygen retained in the most stable structure. Following the data in Supplementary Table 2, the oxygen content at the minimum in Fig. 2c for each of the SSAs is very close to the nominal value of a counterpart model system, placing only O atoms on the surface. Therefore, we can deduce that, in most cases, all oxygens are left as surface oxygen. After the minimum, the uphill part presents a very similar slope in all cases as it corresponds to the same surface oxygen removal process.

These phenomena can be explained by the weaker oxygen binding in the bulk than on the surface³⁴, the lower surface energy of Cu₂O(111) (0.665 J m^{-2}) compared to Cu(111) (1.339 J m^{-2})⁵⁸ and the reconstruction of the Cu₂O surface, which could significantly reduce the energy of the system as shown in Supplementary Note 3 and Supplementary Fig. 5. This observation is in line with a recent experimental study using atomic-scale scanning transmission electron microscopy and electron energy loss spectroscopy techniques, in which the small Cu nanoparticles were completely oxidized to Cu₂O, whereas the large Cu nanoparticles formed Cu@Cu₂O structures⁶.

The distribution of oxygen

After annealing, most of the oxygens are located close to the surface to form the structure of Cu₂O(111) if the remaining number of oxygen

atoms fits the capacity of the surface (Fig. 2d–f). This could be due to the lower surface energy of Cu₂O(111) than Cu(111), which suggests that the formation of Cu₂O on the surface can reduce the energy of the system. Nevertheless, oxygen atoms could also be trapped inside (Supplementary Fig. 10). If the amount of oxygen atoms exceeds the capacity of the surface, the excess oxygen atoms aggregate in the bulk to form Cu₂O (continuous from the surface or in grains), which is consistent with the experimental results²⁹. The oxygen depth profile shown in Fig. 2d for the low SSA model (SSA = 0.034 \AA^{-1} ; Fig. 2e) shows two peaks corresponding to Cu₂O. The peaks indicate the formation of Cu₂O layers (4 atoms per 1.24 \AA for Cu₂O(111)-p(2 × 2)), as Cu₂O has a lower formation energy than Cu_xO (*x* = 4, 6, 8, 64)^{14,58}. Therefore, oxygen atoms tend to aggregate to form Cu₂O to reduce the overall formation energy, and they tend to stay near the surface to reduce the surface energy further. Thus, considering a large-size OD-Cu catalyst containing enough O, the stable static configuration should be one in which some of the oxygen atoms are located on the surface, forming a Cu₂O surface. Meanwhile, excess oxygen causes Cu₂O formed inside the bulk to segregate from the Cu crystal^{6,29}. The diffusion and aggregation of oxygen were also observed in the long-time *NVT* simulation (100 ns) at 300 K (Fig. 3a). The two peaks inside the bulk at 10 ns correspond to the two types of oxygen proposed by a recent X-ray photoelectron spectroscopy study²⁹ (Supplementary Fig. 11).

Oxygen will be eliminated from the surface where the material is in contact with reactants and, as a result, a Cu shell that could affect oxygen diffusion will form. As shown in Fig. 3b, when the top six atomic layers of oxygen were removed from the initial slab, the remaining Cu atoms collapsed immediately, resulting in the formation of a metallic shell on the surface with a similar configuration of face-centred cubic (fcc) copper. At 300 K, no oxygen atom diffuses to the surface after 100 ns equilibration (even after 900 ns at 400 K) as shown in Fig. 3b.

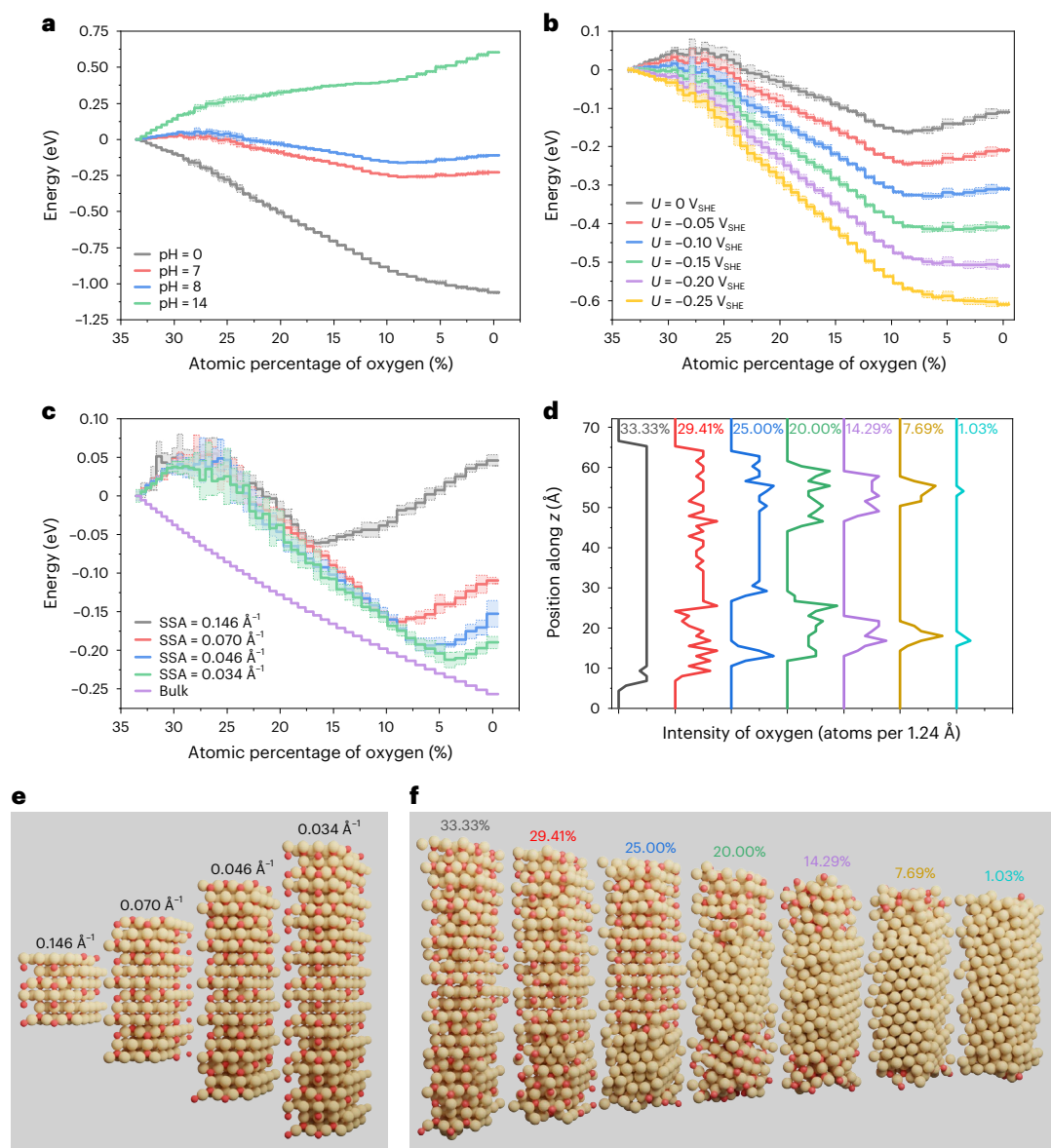


Fig. 2 | The reduction of Cu_2O to Cu under different conditions. **a–c**, The system under different pH values, at $U = 0 \text{ V}_{\text{SHE}}$ and $\text{SSA} = 0.070 \text{ \AA}^{-1}$ (**a**); under different electric potentials versus SHE, at pH = 8 and $\text{SSA} = 0.070 \text{ \AA}^{-1}$ (**b**); and with different SSAs, at pH = 8 and $U = 0 \text{ V}_{\text{SHE}}$ (**c**). The reaction energies were calculated from the average energy of ten randomly sampled OD-Cu slabs (Supplementary Figs. 6–9), using the mean energy during the last 800 ps of equilibration in the annealing simulations (6 ns), and the overall energy was normalized to the reaction energy of per unit of Cu_2O . Dotted lines and transparent regions show the sample standard deviation from these ten

samples. The energy diagram of the bulk is derived from the reduction energy from changing bulk Cu_2O to Cu by using stoichiometry and the DFT static energy instead of MD simulations. **d**, The distribution of oxygen along the z axis for the last frame of OD-Cu ($\text{SSA} = 0.034 \text{ \AA}^{-1}$, sample 1) with different oxygen concentrations. The intensity corresponds to the quantity of oxygen atoms per unit distance along the z axis, and a minor tick interval on the horizontal axis is four atoms per 1.24 \AA , a value derived from a perfect Cu_2O slab model. **e**, The model of the Cu_2O slab with different SSAs; oxygen is red, and copper is tan. **f**, The configurations of OD-Cu structures corresponding to **d**.

This suggests that the diffusion of oxygen is highly constrained in this model. The diffusion of oxygen from inside to the surface was observed in the typical equilibration time in this work, that is, 1 ns, until the equilibration temperature increases to 600 K (the first oxygen appears on the topmost layer in 0.72 ns). Although the formation of a Cu_2O surface is more favourable, the sluggish kinetics of oxygen diffusion could slow the process.

Figure 3c shows the diffusion coefficient of oxygen, D_{O} , in pristine Cu_2O bulk as obtained from the meaningful⁵⁹ data of mean squared displacement (MSD) from 1,200 K to 1,800 K. Both the observed trend and the structure (Supplementary Fig. 12) suggest the presence of two distinct regions within this temperature range. The system exhibits a high degree of ordering from 1,200 K to 1,350 K, while it demonstrates

increased disorder from 1,400 K to 1,800 K. In addition, the two linear relationships show that the transition of Cu_2O from ordered to disordered causes an abrupt change in coefficients, which indicates the effect of latent heat on diffusion. Using the relation between the diffusion coefficient, temperature and energy barrier from Methods equation (12), the apparent energy barrier for O diffusion in Cu_2O is 0.38 eV in the disordered state and 3.32 eV in the ordered state. In addition, nudged elastic band simulations show that the diffusion energy barrier is high in the pristine bulk, but it is greatly reduced by defects (Supplementary Note 4 and Supplementary Fig. 13).

To further evaluate the diffusion of oxygen in the Cu shell case, the simulations for the model in Fig. 3b were run for at least 300 ns at 400–800 K (with 100 K intervals). Below 500 K, no oxygen appears

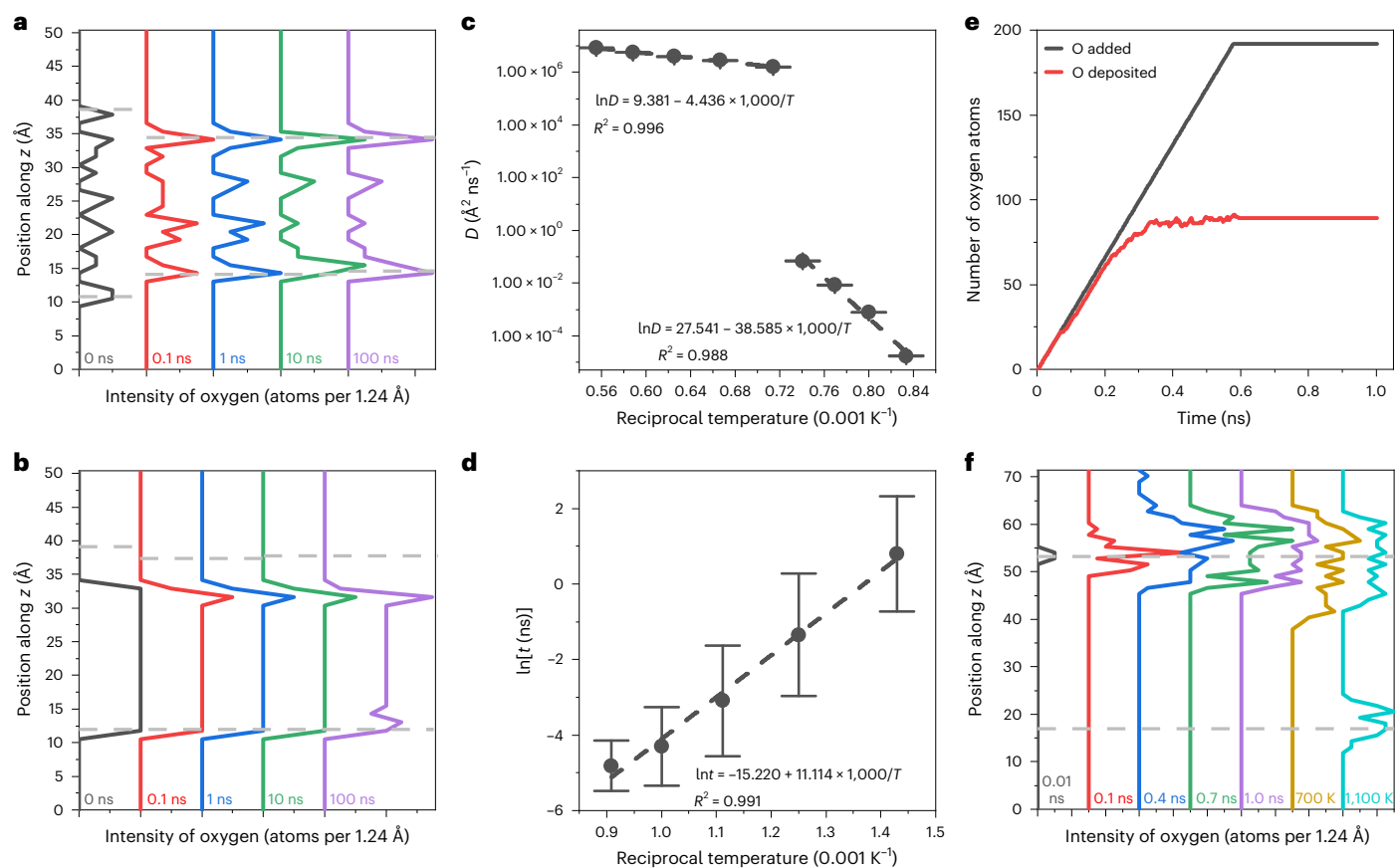


Fig. 3 | The evolution of oxygen distribution and oxygen diffusion kinetics. **a**, Evolution of oxygen distribution for OD-Cu (9.43 at.% O of sample 1 in Fig. 2c). The dashed grey lines indicate the z coordinate of the outermost Cu atom. **b**, Evolution of oxygen distribution for OD-Cu (SSA = 0.070 \AA^{-1}) created by removing oxygen atoms at the topmost atomic layers. The dashed grey lines denote the z coordinate of the outermost Cu atom. **c**, The relation between temperature and oxygen diffusion coefficient (D) from fitting the MSD in perfect Cu_2O bulk. The system exhibits a greater degree of disorder at higher temperatures (1,400 K to 1,800 K) and a higher level of order at lower

temperature (1,200 K to 1,350 K). Error bars show the standard error of the least-squares fitting of the relationship between D and MSD (equation (9)). **d**, The relation between temperature and diffusion time of oxygen from the inside to the surface in the OD-Cu system of **b**. Data are presented as mean values of $\ln(t)$ and error bars show the standard deviation of the $\ln(t)$ of 40 diffusion processes from ten NVT simulations (Supplementary Table 4). **e**, The evolution of the number of added oxygen atoms and deposited oxygen atoms. **f**, Oxygen distribution during the deposition. The dashed lines denote the surface at 0 ns. In **a**, **b** and **f**, a minor tick interval on the horizontal axis is two atoms per 1.24 \AA .

on the surface even after 300 ns. Four surface oxygen atoms appear by 600 K, and the last oxygen atom first emerges at 235.7 ns (diffusion distance along the z axis across the Cu shell, $\sim 6 \text{ \AA}$), while at 900 K this happens even below the nanosecond scale (Supplementary Table 3).

Additionally, an exponential relation between the diffusion time (Supplementary Table 4) and temperature was obtained (Fig. 3d) using ten random initial velocity samples for each temperature from 700 K to 1,100 K. The estimated times for an oxygen atom to diffuse $\sim 6 \text{ \AA}$ are $1.11 \times 10^3 \text{ ns}$, $2.86 \times 10^5 \text{ ns}$ and $3.01 \times 10^9 \text{ ns}$ (3 s) at 500 K, 400 K and 300 K, respectively. The simulations are expected to underestimate the time since a large number of defects are created in the initial configuration. From equation (12), the apparent energy barrier for O diffusion is 0.96 eV. The diffusion path of O in the Cu shell case was further analysed via nudged elastic band simulations. The results show that the diffusion of O from the Cu_2O -Cu interface to the surface roughly involves three distinct processes when a stable Cu shell is formed (Supplementary Note 4 and Supplementary Fig. 14).

Since the diffusion process crosses interfaces, the diffusion time and distance may not follow equation (10) as in a homogeneous phase. To evaluate the relation for diffusion time and distance across the interfaces and Cu shell, slabs with different oxygen layers removed (6 to 14) were simulated with ten samples (Supplementary Table 5). Supplementary Fig. 15 shows that the relationship remains strong although three different processes exist. Thus, the diffusion time for 3.5 nm is

103 s at 300 K based on the square proportionality relationship. The diffusion of oxygen across the Cu shell case is difficult to observe on the timescale of NVT simulations at 300 K, but it certainly can occur on the timescale of experiments. Note that each point of diffusion time in Fig. 3d was obtained from 40 diffusion events observed in ten NVT simulations (Supplementary Table 4). The deviation of the time estimates is still significant (yet smaller than one order of magnitude) for simulated events, and reasonable values on the order of minutes are retrieved in our analysis for an oxygen to diffuse 3.5 nm at 300 K.

The reoxidation of reduced OD-Cu

To assess the effect of air exposure or of a pulsed potential, we simulated the reoxidation process on reduced OD-Cu systems by depositing oxygen atoms at 300 K on the pure Cu reconstructed slab obtained from the system shown in Fig. 2f. The initial model has 384 Cu atoms and, to reach the conversion to Cu_2O , 192 oxygen atoms were gradually added to the system at a rate of one atom per 3 ps, and at an initial velocity of 1 \AA ps^{-1} from 3 \AA above the surface atom to avoid high-speed collision. Initially, the oxygen atoms are adsorbed on the surface, and at about 0.06 ns, all the 20 adatoms sit on the surface. As the content increases, most of the oxygens (103/172) from the deposition source cannot reach the surface due to the repulsion with the surface oxygens. However, after a short time (0.1 ns from the start), the copper atoms are dragged by the surface oxygens, forming a loose structure that allows

the accommodation of more oxygen atoms. Simultaneously, some oxygen atoms penetrate deeper into the bulk. The process stops after 89 oxygen atoms oxidize the material (Fig. 3e). An additional simulation involving 300 deposition atoms gives the same results (Supplementary Fig. 16). The final thickness of the oxide layer is 16.9 Å (Fig. 3f; from 46.3 Å to 63.2 Å on the z axis), in which 6.9 Å of oxide copper species are below the original surface (upper dashed line in Fig. 3f, at 53.2 Å), indicating the diffusion of oxygen into the interior, and 10 Å are above the original surface, corresponding to the outward displacement of Cu. This agrees with the hypothesis by experimentalists that only the near surface layers are oxidic⁶⁰. In the oxidation simulation, the oxygen rapidly diffuses from the surface to 6.9 Å inside the surface, unlike in the reduction process, where the oxygen diffusion from inside to the surface was not observed at 300 K when pure copper formed on the surface. The reason may be that copper has enough space to move on the surface. Again, when the oxygen diffuses to 6.9 Å under the surface, the shell structure prevents the diffusion of oxygen, in conjunction with the difficulty of depositing more oxygen to the surface, and deep oxidation takes longer.

Moreover, the composition of oxide layers (atoms above the deepest oxygen) on the surface is $\text{Cu}_{79}\text{O}_{89}$ ($\text{Cu}_{71}\text{O}_{89}$ for the 300 atom case), which indicates that the surface Cu is mainly Cu(II). After annealing at 700 K (note that 1 ns at 700 K is equivalent to ~ 1.6 s equilibration at 300 K, considering only the oxygen diffusion time from the Cu shell model; the same consideration is applied below), the composition changes to $\text{Cu}_{139}\text{O}_{89}$, which includes both Cu(II) and Cu(I). The thickness changes from 17 Å to 23 Å, which is comparable to the experimental findings ($\sim 2\text{--}3$ nm)^{6,29,60}. After annealing at 1,100 K (the 1 ns at 1,100 K is equivalent to ~ 502.6 s equilibration at 300 K), some of the oxygen atoms diffuse from the upper surface to the bottom surface and the composition changes to $\text{Cu}_{117}\text{O}_{60}$ (upper) and $\text{Cu}_{56}\text{O}_{29}$ (bottom), both of which are almost Cu(I). Note that the timescale obtained here is based on the relation between temperature and time for the Cu shell model in Fig. 3d, which has limited statistics.

The active site via graph theory

Considering typical experimental settings, a Cu_2O nanoparticle 20 nm (ref. 61) in diameter, at pH 8 and $U \leq -0.3 V_{\text{RHE}}$, should be reduced to pure Cu. We used a 3,240 atom Cu slab derived by removing all oxygens from a 30-atomic-layer $\text{Cu}_2\text{O}(\text{111})\text{-p}(9 \times 9)$ (equivalent to a 7.1 nm nanoparticle in SSA) to simulate the high roughness of the surface. After equilibration, the slab structure (equivalent to a 4.4 nm nanoparticle in SSA) forms a distorted configuration with an average coordination number of 9.08, with a decay controlled by an error function¹⁴ and an average distance of 2.58 Å (Supplementary Fig. 17). Compared to the coordination number of 12 and the Cu–Cu distance of 2.56 Å in bulk Cu, the structure has low coordination and is stretched less than 1%. The 2,861 active sites are detected via a Delaunay triangulation sampling⁶² of the last frame of the simulation, and there are 16 different active sites based on the isomorphism analysis⁶³, as shown in Fig. 4a. The active sites are further categorized to eight classes for analysis. Classes I, II and III account for the most abundant, 13.28%, 49.98% and 27.19% populations, corresponding to atop, fcc/hcp and bridge sites, respectively, and the Cu atoms in these sites could be under-coordinated. Class IV (2.48%) also represents three coordinated sites, but unlike the hcp/fcc sites, two of the Cu atoms are not interconnected. Classes V (4.89%), VI (1.12%) and VII (0.59%) represent four coordinated sites, where VI is similar to the hollow site on Cu(100), while the other two categories are connected in a slightly distorted way: V, where a pair of diagonal atoms bonded, and VII, where one of the four copper atoms that make up the square is connected to only one other. The last nine active sites together represent only 0.45% of the number of total active sites, which are oxygen-adsorbed near steps with high coordination numbers (three-dimensional structures are presented in Supplementary Fig. 18); thus, they are categorized as class VIII for analysis.

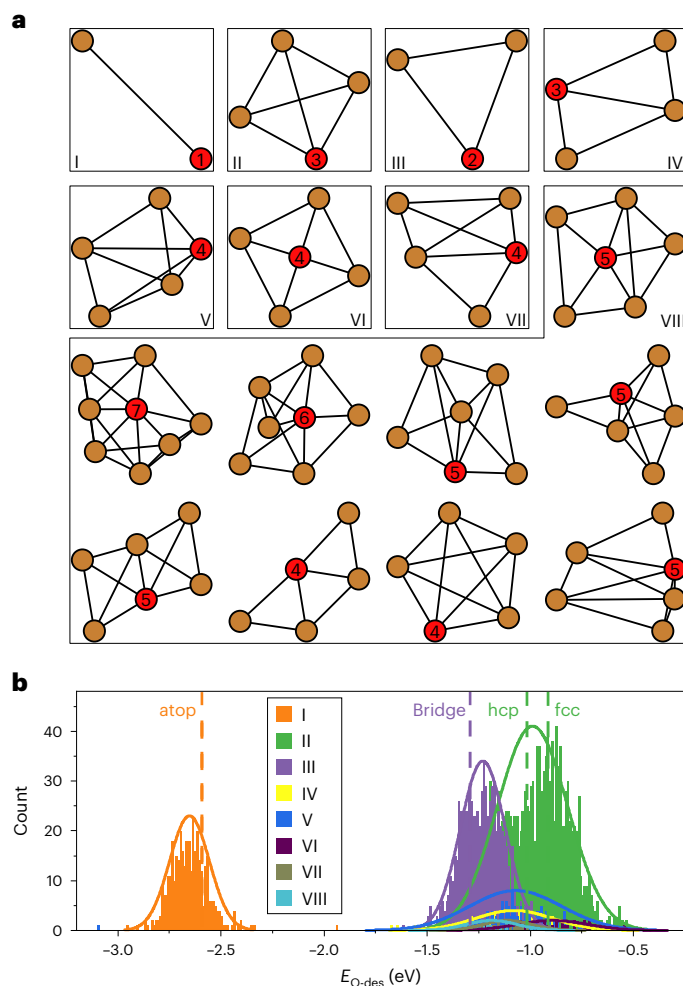


Fig. 4 | The active sites identified via graph theory and the distribution of the oxygen desorption energy. **a**, Graph representation of oxygen (red) and its first neighbouring copper atoms (brown). The number is the coordination number of oxygen, while the geometric configurations are presented in Supplementary Fig. 18. **b**, Distribution of oxygen desorption energy ($E_{\text{O-des}}$) for different types of active sites at pH 0 and $U = 0 V_{\text{SHE}}$. The solid curves show the Gaussian distribution, and the dashed lines are the desorption energies of oxygen on the corresponding active sites on Cu(III).

The reconstructed surface gives a wide distribution of oxygen desorption energies from -0.51 eV to -3.10 eV at pH 0 and $U = 0 V_{\text{SHE}}$. At pH 8 and $U = 0 V_{\text{SHE}}$, 25.2% of the oxygen desorption is endothermic (Supplementary Fig. 19), and all the oxygens are removed from the surface at computational reduction potentials more negative than $-0.22 V_{\text{SHE}}$ ($+0.26 V_{\text{RHE}}$). Instead, at pH 14, the computational reduction potential needs to be lower than $-0.58 V_{\text{SHE}}$ ($+0.26 V_{\text{RHE}}$) to remove the residual oxygen completely. Thus, the residual oxygen on the surface can exist under certain experimental conditions, and the amount of residual oxygen can be fine-tuned by controlling the reaction conditions (such as applying pulsed potentials).

Discussion

The computational framework employed here provides a systematic approach for understanding the material changes from bulk to surface during operando conditions, not only from a thermodynamic perspective but also from a kinetic standpoint. The simulations point to an OD-Cu oxygen content at zero electric potential versus SHE that is highly dependent on the pH, with Cu_2O reduced to Cu under strongly acidic conditions while Cu_2O is stable under strongly basic conditions. Under near-neutral conditions at zero electric potential

versus SHE, the Cu₂O with a SSA of 0.146 Å⁻¹ retains 16.5 at.% of the oxygen. The pH and electric potential dependence were obtained via the computational hydrogen electrode model and could benefit from further refined modelling of the environment. The SSA of the Cu₂O particle affects the reduction degree: the lower the SSA, the higher the reduction degree. Depending on the size distribution of the Cu₂O particles, the time windows for the simultaneous presence of oxidic and metallic surfaces are different. While a strong reduction potential could lead to the complete reduction of Cu₂O, the sluggish kinetics of oxygen diffusion from inside to the surface causes the process to take a long time to complete (from seconds to hours, depending on the size), which agrees with experimental observations⁶⁰, and the diffusion roughly involves three distinct processes: diffusion across the Cu₂O–Cu interface, inside the Cu and from the subsurface to the surface. Compared to the most recent experiments²⁹, the evidence from grazing incidence XPS can be seen as being originated by defect species for O close to the surface and by the interstitial defect species, and we also found these configurations in our simulations.

As for the reducing/oxidating processes, our computational results match the experimental values, even those regarding the timescale of the events⁶. X-ray absorption spectroscopy combined with electron energy loss spectroscopy analysis demonstrates the metallic nature of the 7 nm nanoparticle after 30 min at $-0.8 V_{\text{RHE}}$. After 1 h, the extended X-ray absorption fine structure (EXAFS) of these particles retrieves a coordination number for Cu of 8.1 ± 1.6 . As EXAFS corresponds to an average of bulk and surface atoms, the observation means that the Cu catalyst contains a large fraction of under-coordinated sites under steady-state conditions. In our calculation for the equivalent system, we find that the average coordination number is 9.08, and complete oxygen depletion is achieved in 1.7 min (computational deviation below one order of magnitude), within the same range as that observed experimentally. In addition, the small Cu structures (7 nm) fully reoxidize after 5 h of air exposure⁶, while the larger structures form Cu@Cu₂O shell structures (2 nm oxide shell). This also agrees with our result that the large-size structures have a lower O content, and with a computed reoxidation shell of 2.3 nm after 700 K annealing.

EXAFS analysis shows that the removal of oxygens results in materials with significant degrees of disorder. Electrocatalytic experiments show that the disordered grains are responsible for the under-coordinated sites active in the CO₂RR. In experiments with air exposure, these defects can react with O₂, leading to the spontaneous incorporation of oxygen in the lattice. In our simulations, once O₂ is split, the penetration of O into these disordered layers is rather fast, with the oxidation layer reaching saturation within 0.4 ns when depositing one O atom per 3 ps.

In conclusion, the structures of OD-Cu during the reduction process under different conditions were systematically studied via large-scale MD at first-principles accuracy with a NNP (r.m.s.e. of 4.58 meV per atom with respect to PBE-D2). The oxygen concentration of the OD-Cu materials strongly depends on the history of the sample and the reaction conditions: the higher the pH/potential/SSA, the higher the oxygen concentration in the most stable OD-Cu configuration. The oxygen atoms tend to aggregate to form Cu₂O on the surface and inside the bulk to reduce the energy by lowering the formation energy and surface energy instead of being distributed uniformly. In long electrochemical experiments, OD-Cu materials reduce to Cu, but a considerable amount of time (several seconds to hours, with diffusion time proportional to the square of the distance and exponential to the reciprocal of temperature) is required to remove all the trapped oxygen. Moreover, the highly reconstructed Cu surface yields sites with widely distributed oxygen adsorption energy values, although the residual oxygen will be reduced under common experimental conditions. These results not only reveal the dynamics of the stable structure of OD-Cu under

different experimental conditions but also give insight into the mechanism of the reduction of OD-Cu and the limits for fine-tuning by controlling experimental conditions.

Methods

Ab initio simulations

The DFT simulations were performed using the Vienna Ab initio Simulation Package^{64,65} with the Perdew–Burke–Ernzerhof functional⁴⁶ and our refitted DFT-D2 van der Waals parameters^{47–49}. For valence electrons, a plane-wave basis set was adopted with an energy cut-off of 450 eV, and the ionic cores were described with the projector augmented-wave method. The Brillouin zone was sampled using gamma-centred Monkhorst–Pack with a k-point spacing of $0.03 \times 2\pi \text{ \AA}^{-1}$ for the Cu and Cu_xO system, and $0.05 \times 2\pi \text{ \AA}^{-1}$ for the Cu₂O system, with an accuracy converging to 1.4 meV per atom (using the energy from the lowest k-point spacing as a reference), as shown in Supplementary Fig. 20. The numbers of k points along different axes for different cells were generated using vaspkit (ref. 66) with the aforementioned k-point spacing, where the k-point spacing along the *i* axis is $\frac{b_i \times 2\pi}{N_i}$. In addition, only one k point is employed for the axis along the normal direction of the surface of the slab model. Previous DFT tests for the Cu₂O demonstrated that no significant contribution of self-interaction error is present for these materials¹⁴. The total energy was converged to an accuracy of 1×10^{-6} eV, and a force tolerance of 0.03 eV \AA^{-1} was used in all structure optimizations.

A time step of 3 fs was chosen for MD simulations, which allows at least 16 samples within a normal Cu–O vibration period according to our previous test¹⁴. The AIMD was performed using the canonical ensemble (*NVT*) with a Nosé–Hoover thermostat^{67,68}. For Cu, fcc, body-centred cubic (bcc) and two hcp bulk structures with supercells of $1 \times 1 \times 1$, $2 \times 2 \times 2$, $3 \times 3 \times 3$ and $4 \times 4 \times 4$ were used for the AIMD simulation at temperatures of 300 K, 500 K and 700 K. The (111), (110), (100) and (211) surfaces of the fcc bulk with five and eight layers were simulated at 300 K and 700 K. Each AIMD simulation was run for 300 steps, and 1,398 bulk structures and 690 surface structures were chosen, returning an initial dataset for copper of 2,088 data points. For Cu₂O, bulks with supercells of $1 \times 1 \times 1$, $2 \times 1 \times 1$, $2 \times 2 \times 2$ and $3 \times 3 \times 3$ were used to run the AIMD at 700 K and 1,550 K. In addition, the (111), (110), (100) and (211) surfaces with six layers were simulated at 1,550 K. These simulations gave 3,600 structures for the initial dataset for Cu₂O.

For the initial dataset of Cu_xO, the data points were generated via the optimization of structures of randomly adsorbing oxygen on Cu surfaces or removing oxygen from Cu₂O bulks and surfaces. One to four oxygen atoms were randomly adsorbed on a (100)-p(2 × 2), (110)-p(3 × 2), (111)-p(3 × 3) and (211)-p(1 × 3) surface five times, resulting in 80 data points. The 2 × 2 bulk and (111), (110), (100) and (211) unit surfaces, and the (111)-p(2 × 2), (110)-p(4 × 2), (100)-p(4 × 2) and (211)-p(1 × 4) of Cu₂O were used to generate the structure of Cu_xO. The number of randomly removed oxygen atoms increased from one to the pristine number of oxygens in the models minus one unit. The oxygen atoms were randomly removed five times, giving the 725 data points. In total, the initial dataset of Cu_xO consisted of 805 data points.

Neural network potential

The Behler–Parrinello-type HDNNP (ref. 50) was constructed using n2p2 (refs. 51,53). The NNPs were trained via multistream extended Kalman filter algorithms using energies and forces. The following radial symmetry function and angular symmetry function were employed to describe the local atomic environment with the parameters shown in Supplementary Tables 6 and 7:

$$G_i^{\text{rad}} = \sum_{j \neq i} e^{-\pi(r_{ij}-r_s)^2} f_c(r_{ij}) \quad (1)$$

$$G_i^{\text{ang}} = 2^{1-\zeta} \sum_{\substack{j, k \neq i \\ j < k}} (1 + \lambda \cos \theta_{ijk})^\zeta e^{-\eta(r_{ij}^2 + r_{ik}^2 + r_{jk}^2)} f_c(r_{ij}) f_c(r_{ik}) f_c(r_{jk}) \quad (2)$$

where

$$f_c(r_{ij}) = \begin{cases} 0.5 \left(\cos \frac{\pi r_{ij}}{r_c} + 1 \right) & \text{for } r_{ij} \leq r_c \\ 0 & \text{otherwise.} \end{cases} \quad (3)$$

r_{ij} is the distance between atoms i and j ; η and r_s control the width and center, respectively, of the Gaussian function. θ_{ijk} is angle centered at atom i , angular resolution is provided by the parameter ζ , λ shifts the maxima of the cosine function to different θ_{ijk} , r_c is cutoff radius. In total, 98 symmetry functions were used, 40 of which were for oxygen and 58 of which were for Cu (Supplementary Tables 6 and 7). Thus, neural networks with an architecture of 98–15–15–1 were employed, that is, 98 neurons for the input layer to represent the structure, two hidden layers with 15 neurons each and 1 neuron for the output layer. The dataset was divided into a training set (90% data) and a test set (10% data).

To improve the quality of the NNPs, an expanded dataset was built via active learning using a modified framework based on RuNNerActiveLearn (refs. 69–71). The active learning procedure was stopped when no extrapolation was found in the runs, all energy differences between the two NNPs were lower than five times the r.m.s.e. of the energy and all force differences between the two NNPs were lower than ten times the r.m.s.e. of the forces. If the potential is not applicable to the three validation systems, the active learning is launched again, and the temperature of NN-MDs is increased to gain structural diversity. Further tests regarding the lattice constant and melting point are presented in Supplementary Note 1 and Supplementary Figs. 21 and 22.

NN-MD simulations

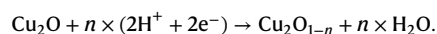
The simulations of NN-MD were performed using the LAMMPS code⁵² with the NNP interface from n2p2 (refs. 51,53). For equilibration, the simulations were run for 1 ns at the indicated temperature. For annealing, the simulations were run at 1,100 K for 1 ns; then the systems were cooled to 300 K in 4 ns with a cooling rate of 0.2 K ps⁻¹ and finally another 1 ns for equilibration at 300 K. The canonical (*NVT*) ensemble simulations were modelled with the Nosé–Hoover thermostat for surface systems, and the Nosé–Hoover thermostat and barostat were employed for isobaric–isothermic (*NPT*) ensemble simulations of the bulk systems⁷². To ensure a thorough exploration of the configuration space and to avoid artefacts arising from the random sampling, the reduction process for each slab was simulated with ten random samplings (that is, ten randomized indexed lists for sequential oxygen removal), which contain 1,960 annealing processes, each with a time length of 6 ns. Then, the mean values from these samples were used, and the sample standard deviation was analysed to quantify errors due to random samplings. In addition, ten NNPs were trained to test the robustness of the current NNP and the dataset, and all the different parameters of the annealing were extensively tested, as shown in Supplementary Note 2 and Supplementary Figs. 23–27.

The energy minimization of the adsorption of oxygen (where all the slab atoms are fixed to simulate the surface under equilibrium) was stopped when the energy change converged to 10⁻⁷ of the total energy (-0.01 eV). Active sites were detected via Delaunay triangulation sampling of the last frame of the equilibration simulation, and the different active sites were obtained based on the isomorphism analysis of the first-order graphs (only the first neighbours of oxygen and their connections were considered) on the minimized configurations. In this representation, the fcc and hcp sites are identical, since increasing to second order would result in an excessive number of different unique sites, making the analysis difficult. Climbing image nudged elastic band method⁷³ implemented in the LAMMPS REPLIC package was used to

search the transition state of the diffusions with a force tolerance of 0.03 eV Å⁻¹. For oxygen diffusion in the Cu shell case, the structures from sampling 1 with a SSA of 0.070 Å⁻¹ were used. The configurations taken 30 ps before the oxygen atom appears on the surface were minimized and employed as the initial state. The bottom 15 atomic layers were fixed, and the upper 12 atomic layers were relaxed.

Reaction energy and desorption energy

The reduction of Cu₂O to OD-Cu is considered to occur as follows, where e⁻ is an electron:



Then, the reaction energies at U versus SHE were calculated by

$$\Delta E = \langle E_{\text{Cu}_2\text{O}_{1-n}} \rangle + nE_{\text{H}_2\text{O}} - \langle E_{\text{Cu}_2\text{O}} \rangle - nE_{\text{H}_2} + n \times 2k_B T \times \ln(10) \times \text{pH} + n \times 2 \times e \times U \quad (4)$$

where $\langle E_{\text{Cu}_2\text{O}_{1-n}} \rangle$ and $\langle E_{\text{Cu}_2\text{O}} \rangle$ are the mean potential energy of Cu₂O_{1- n} ($0 \leq n \leq 1$) and Cu₂O, respectively, in the last 800 ps equilibration of the annealing simulation; $E_{\text{H}_2\text{O}}$ and E_{H_2} are the energy of H₂O and H₂, respectively, from the DFT simulation; T is temperature; and $(1-n)/(3-n)$ equals the atomic content of oxygen in the OD-Cu.

The desorption energy of oxygen is calculated as follows:

$$\text{For } \text{O}^* + 2\text{H}^+ + 2\text{e}^- \rightarrow * + \text{H}_2\text{O}, \\ E_{\text{O-des}} = E_* + E_{\text{H}_2\text{O}} - E_{\text{H}_2} - E_{\text{O}^*} + 2k_B T \times \ln(10) \times \text{pH} + 2 \times e \times U \quad (5)$$

where E_* and E_{O^*} are the energies of the slab and the adsorption configuration, respectively, from the NNP.

Specific surface area

The SSA was calculated as follows:

$$\text{SSA} = \frac{\text{surface area}}{\text{volume}} \quad (6)$$

For the slab model

$$\text{SSA} = \frac{2A}{Ad} = \frac{2}{d} \quad (7)$$

The nanoparticle was treated as a sphere:

$$\text{SSA} = \frac{4\pi r^2}{\frac{4}{3}\pi r^3} = \frac{3}{r} = \frac{6}{D_p} \quad (8)$$

Here, A is the cross-sectional area of the slab, d is the thickness of the slab, r is the radius of the nanoparticle and D_p is the diameter of the nanoparticle.

Diffusion coefficient

The Einstein relation associates the self-diffusion coefficient, D , with the mean square displacement (MSD) as a function of observation time.

$$D = \frac{1}{2d} \lim_{t \rightarrow \infty} \frac{\langle [r(t_0 + t) - r(t_0)]^2 \rangle}{t} \quad (9)$$

where D is the self-diffusion coefficient, d is the dimensionality of the system, t is time, t_0 is time zero and $\langle [r(t_0 + t) - r(t_0)]^2 \rangle$ is the MSD. The diffusion coefficient is fitted⁷⁴ on the MSD of displacement time length (the lag time) from 0.1 times the simulation time to 0.5 times the simulation times (Supplementary Fig. 12) to avoid the ballistic trajectory in the short-time region and increased noise in the long-time region⁵⁹. To obtain reasonable MSD values, 3 × 3 × 3 Cu₂O bulk was

equilibrated for 1,500 ns (1,200 K), 600 ns (1,250 K, 1,300 K), 100 ns (1,350 K), 10 ns (1,400 K, 1,500 K) or 2 ns (1,600 K, 1,700 K, 1,800 K).

From the above, the diffusion time is as follows:

$$t = \frac{r^2}{2dD} \quad (10)$$

Furthermore, for solid and liquid⁷⁵, the diffusion coefficient and temperature have a relationship following the Arrhenius equation as follows:

$$D(T) = D_0 \exp\left(\frac{-E_a}{k_B T}\right) \quad (11)$$

$$\ln D(T) = \ln D_0 - \frac{E_a}{k_B} \times \frac{1}{T} \quad (12)$$

Then, the relationship between diffusion time and temperature is as follows:

$$\ln[t(T)] = \ln \frac{r^2}{2dD_0} + \frac{E_a}{k_B} \times \frac{1}{T} \quad (13)$$

For the Cu shell model built by removing the top six atomic oxygen layers, because of its constrained diffusion nature, the diffusion coefficient can hardly be fitted using the MSD (equation (9)), but the relationship between diffusion time and temperature still follows equation (13). Thus, ten samplings with random initial velocities were simulated for each temperature from 700 K to 1,100 K. Four oxygen diffusion processes were traced and treated as independent for each simulation, as the diffusion time is related only to the diffusion distance at constant temperature, theoretically. The average value was used as the diffusion time for the fitting. All the times, the average and the sample standard derivation, *s*, are shown in Supplementary Table 4.

Data availability

The source of the initial dataset, the final dataset, the machine learning potential files, the MD trajectories (reconstitution, coexistence, reduction, deposition, diffusion and tests of annealing parameters), the energy minimization of the oxygen adsorption and nudged elastic band simulations are available on the ioChem-BD database⁷⁶ (<https://doi.org/10.19061/iochem-bd-6-228>).

References

- Birdja, Y. Y. et al. Advances and challenges in understanding the electrocatalytic conversion of carbon dioxide to fuels. *Nat. Energy* **4**, 732–745 (2019).
- Wang, G. et al. Electrocatalysis for CO₂ conversion: from fundamentals to value-added products. *Chem. Soc. Rev.* **50**, 4993–5061 (2021).
- Das, S. et al. Core-shell structured catalysts for thermocatalytic, photocatalytic, and electrocatalytic conversion of CO₂. *Chem. Soc. Rev.* **49**, 2937–3004 (2020).
- Hori, Y., Murata, A. & Takahashi, R. Formation of hydrocarbons in the electrochemical reduction of carbon dioxide at a copper electrode in aqueous solution. *J. Chem. Soc. Faraday Trans. 1* **85**, 2309–2326 (1989).
- Zhou, Y. et al. Long-chain hydrocarbons by CO₂ electroreduction using polarized nickel catalysts. *Nat. Catal.* **5**, 545–554 (2022).
- Yang, Y. et al. Operando studies reveal active Cu nanograins for CO₂ electroreduction. *Nature* **614**, 262–269 (2023).
- Ma, M., Djanashvili, K. & Smith, W. A. Controllable hydrocarbon formation from the electrochemical reduction of CO₂ over Cu nanowire arrays. *Angew. Chem. Int. Ed.* **55**, 6680–6684 (2016).
- Varela, A. S., Kroschel, M., Reier, T. & Strasser, P. Controlling the selectivity of CO₂ electroreduction on copper: the effect of the electrolyte concentration and the importance of the local pH. *Catal. Today* **260**, 8–13 (2016).
- Pander, J. E. et al. Understanding the heterogeneous electrocatalytic reduction of carbon dioxide on oxide-derived catalysts. *ChemElectroChem* **5**, 219–237 (2018).
- Ma, S. et al. One-step electrosynthesis of ethylene and ethanol from CO₂ in an alkaline electrolyzer. *J. Power Sources* **301**, 219–228 (2016).
- Kas, R. et al. Electrochemical CO₂ reduction on Cu₂O-derived copper nanoparticles: controlling the catalytic selectivity of hydrocarbons. *Phys. Chem. Chem. Phys.* **16**, 12194–12201 (2014).
- Nitopi, S. et al. Progress and perspectives of electrochemical CO₂ reduction on copper in aqueous electrolyte. *Chem. Rev.* **119**, 7610–7672 (2019).
- Bagger, A., Ju, W., Varela, A. S., Strasser, P. & Rossmeisl, J. Electrochemical CO₂ reduction: classifying Cu facets. *ACS Catal.* **9**, 7894–7899 (2019).
- Dattila, F., García-Muelas, R. & López, N. Active and selective ensembles in oxide-derived copper catalysts for CO₂ reduction. *ACS Energy Lett.* **5**, 3176–3184 (2020).
- Lin, S. C. et al. Operando time-resolved X-ray absorption spectroscopy reveals the chemical nature enabling highly selective CO₂ reduction. *Nat. Commun.* **11**, 3525 (2020).
- Arán-Ais, R. M., Scholten, F., Kunze, S., Rizo, R. & Roldan Cuenya, B. The role of in situ generated morphological motifs and Cu(I) species in C₂₊ product selectivity during CO₂ pulsed electroreduction. *Nat. Energy* **5**, 317–325 (2020).
- Zhou, Y. et al. Dopant-induced electron localization drives CO₂ reduction to C₂ hydrocarbons. *Nat. Chem.* **10**, 974–980 (2018).
- Jeong, H. M. et al. Atomic-scale spacing between copper facets for the electrochemical reduction of carbon dioxide. *Adv. Energy Mater.* **10**, 1903423 (2020).
- Gao, D., Aran-Ais, R. M., Jeon, H. S. & Roldan Cuenya, B. Rational catalyst and electrolyte design for CO₂ electroreduction towards multicarbon products. *Nat. Catal.* **2**, 198–210 (2019).
- Li, C. W. & Kanan, M. W. CO₂ reduction at low overpotential on Cu electrodes resulting from the reduction of thick Cu₂O films. *J. Am. Chem. Soc.* **134**, 7231–7234 (2012).
- Zhu, C. et al. Product-specific active site motifs of Cu for electrochemical CO₂ reduction. *Chem* **7**, 406–420 (2021).
- Lum, Y. & Ager, J. W. Evidence for product-specific active sites on oxide-derived Cu catalysts for electrochemical CO₂ reduction. *Nat. Catal.* **2**, 86–93 (2019).
- Jiang, K. et al. Metal ion cycling of Cu foil for selective C–C coupling in electrochemical CO₂ reduction. *Nat. Catal.* **1**, 111–119 (2018).
- Kim, D., Kley, C. S., Li, Y. & Yang, P. Copper nanoparticle ensembles for selective electroreduction of CO₂ to C₂–C₃ products. *Proc. Natl Acad. Sci. USA* **114**, 10560–10565 (2017).
- Dutta, A., Rahaman, M., Luedi, N. C., Mohos, M. & Broekmann, P. Morphology matters: tuning the product distribution of CO₂ electroreduction on oxide-derived Cu foam catalysts. *ACS Catal.* **6**, 3804–3814 (2016).
- Reske, R., Mistry, H., Beharid, F., Roldan Cuenya, B. & Strasser, P. Particle size effects in the catalytic electroreduction of CO₂ on Cu nanoparticles. *J. Am. Chem. Soc.* **136**, 6978–6986 (2014).
- Louidice, A. et al. Tailoring copper nanocrystals towards C₂ products in electrochemical CO₂ reduction. *Angew. Chem. Int. Ed.* **55**, 5789–5792 (2016).
- Kim, D., Resasco, J., Yu, Y., Asiri, A. M. & Yang, P. Synergistic geometric and electronic effects for electrochemical reduction of carbon dioxide using gold-copper bimetallic nanoparticles. *Nat. Commun.* **5**, 4948 (2014).

29. Wang, H. Y. et al. Direct evidence of subsurface oxygen formation in oxide-derived Cu by X-ray photoelectron spectroscopy. *Angew. Chem. Int. Ed.* **61**, e202111021 (2022).
30. Velasco-Velez, J. J. et al. Revealing the active phase of copper during the electroreduction of CO₂ in aqueous electrolyte by correlating *in situ* X-ray spectroscopy and *in situ* electron microscopy. *ACS Energy Lett.* **5**, 2106–2111 (2020).
31. Ren, D. et al. Selective electrochemical reduction of carbon dioxide to ethylene and ethanol on copper(I) oxide catalysts. *ACS Catal.* **5**, 2814–2821 (2015).
32. Lum, Y. & Ager, J. W. Stability of residual oxides in oxide-derived copper catalysts for electrochemical CO₂ reduction investigated with ¹⁸O labeling. *Angew. Chem. Int. Ed.* **57**, 551–554 (2018).
33. Garza, A. J., Bell, A. T. & Head-Gordon, M. Is subsurface oxygen necessary for the electrochemical reduction of CO₂ on copper? *J. Phys. Chem. Lett.* **9**, 601–606 (2018).
34. Fields, M., Hong, X., Nørskov, J. K. & Chan, K. Role of subsurface oxygen on Cu surfaces for CO₂ electrochemical reduction. *J. Phys. Chem. C* **122**, 16209–16215 (2018).
35. Chen, C. et al. The *in situ* study of surface species and structures of oxide-derived copper catalysts for electrochemical CO₂ reduction. *Chem. Sci.* **12**, 5938–5943 (2021).
36. Lee, S. H. et al. Oxidation state and surface reconstruction of Cu under CO₂ reduction conditions from *in situ* X-ray characterization. *J. Am. Chem. Soc.* **143**, 588–592 (2021).
37. Mandal, L. et al. Investigating the role of copper oxide in electrochemical CO₂ reduction in real time. *ACS Appl. Mater. Interfaces* **10**, 8574–8584 (2018).
38. Scott, S. B. et al. Absence of oxidized phases in Cu under CO reduction conditions. *ACS Energy Lett.* **4**, 803–804 (2019).
39. Beverskog, B. & Puigdomenech, I. Revised Pourbaix diagrams for copper at 25 to 300 °C. *J. Electrochem. Soc.* **144**, 3476–3483 (1997).
40. Favaro, M. et al. Subsurface oxide plays a critical role in CO₂ activation by Cu(111) surfaces to form chemisorbed CO₂, the first step in reduction of CO₂. *Proc. Natl Acad. Sci. USA* **114**, 6706–6711 (2017).
41. Eilert, A. et al. Subsurface oxygen in oxide-derived copper electrocatalysts for carbon dioxide reduction. *J. Phys. Chem. Lett.* **8**, 285–290 (2017).
42. He, M. et al. Oxygen induced promotion of electrochemical reduction of CO₂ via Co-electrolysis. *Nat. Commun.* **11**, 3844 (2020).
43. Liu, G. et al. CO₂ reduction on pure Cu produces only H₂ after subsurface O is depleted: theory and experiment. *Proc. Natl Acad. Sci. USA* **118**, e2012649118 (2021).
44. Gauthier, J. A., Stenlid, J. H., Abild-Pedersen, F., Head-Gordon, M. & Bell, A. T. The role of roughening to enhance selectivity to C₂₊ products during CO₂ electroreduction on copper. *ACS Energy Lett.* **6**, 3252–3260 (2021).
45. Cheng, D. et al. The nature of active sites for carbon dioxide electroreduction over oxide-derived copper catalysts. *Nat. Commun.* **12**, 395 (2021).
46. Perdew, J. P., Burke, K. & Ernzerhof, M. Generalized gradient approximation made simple. *Phys. Rev. Lett.* **77**, 3865–3868 (1996).
47. Grimme, S. Semiempirical GGA-type density functional constructed with a long-range dispersion correction. *J. Comput. Chem.* **27**, 1787–1799 (2006).
48. Bučko, T., Hafner, J., Lebègue, S. & Ángyán, J. G. Improved description of the structure of molecular and layered crystals: *ab initio* DFT calculations with van der Waals corrections. *J. Phys. Chem. A* **114**, 11814–11824 (2010).
49. Almora-Barrios, N., Carchini, G., Błoński, P. & López, N. Costless derivation of dispersion coefficients for metal surfaces. *J. Chem. Theory Comput.* **10**, 5002–5009 (2014).
50. Behler, J. Atom-centered symmetry functions for constructing high-dimensional neural network potentials. *J. Chem. Phys.* **134**, 074106 (2011).
51. Singraber, A., Morawietz, T., Behler, J. & Dellago, C. Parallel multistream training of high-dimensional neural network potentials. *J. Chem. Theory Comput.* **15**, 3075–3092 (2019).
52. Thompson, A. P. et al. LAMMPS - a flexible simulation tool for particle-based materials modeling at the atomic, meso, and continuum scales. *Comput. Phys. Commun.* **271**, 108171 (2022).
53. Singraber, A., Behler, J. & Dellago, C. Library-based LAMMPS implementation of high-dimensional neural network potentials. *J. Chem. Theory Comput.* **15**, 1827–1840 (2019).
54. Behler, J. Four generations of high-dimensional neural network potentials. *Chem. Rev.* **121**, 10037–10072 (2021).
55. Morrow, J. D., Gardner, J. L. A. & Deringer, V. L. How to validate machine-learned interatomic potentials. *J. Chem. Phys.* **158**, 121501 (2023).
56. Nørskov, J. K. et al. Origin of the overpotential for oxygen reduction at a fuel-cell cathode. *J. Phys. Chem. B* **108**, 17886–17892 (2004).
57. García de Arquer, F. P. et al. CO₂ electrolysis to multicarbon products at activities greater than 1 A cm⁻². *Science* **367**, 661–666 (2020).
58. Jain, A. et al. Commentary: the Materials Project: a materials genome approach to accelerating materials innovation. *APL Mater.* **1**, 011002 (2013).
59. Maginn, E. J., Messerly, R. A., Carlson, D. J., Roe, D. R. & Elliot, J. R. Best practices for computing transport properties 1. Self-diffusivity and viscosity from equilibrium molecular dynamics [article v1.0]. *Living J. Comput. Mol. Sci.* **1**, 6324 (2018).
60. Timoshenko, J. et al. Steering the structure and selectivity of CO₂ electroreduction catalysts by potential pulses. *Nat. Catal.* **5**, 259–267 (2022).
61. Jung, H. et al. Electrochemical fragmentation of Cu₂O nanoparticles enhancing selective C–C coupling from CO₂ reduction reaction. *J. Am. Chem. Soc.* **141**, 4624–4633 (2019).
62. Ong, S. P. et al. Python Materials Genomics (pymatgen): a robust, open-source Python library for materials analysis. *Comput. Mater. Sci.* **68**, 314–319 (2013).
63. Deshpande, S., Maxson, T. & Greeley, J. Graph theory approach to determine configurations of multidentate and high coverage adsorbates for heterogeneous catalysis. *npj Comput. Mater.* **6**, 79 (2020).
64. Kresse, G. & Furthmüller, J. Efficient iterative schemes for *ab initio* total-energy calculations using a plane-wave basis set. *Phys. Rev. B* **54**, 11169–11186 (1996).
65. Kresse, G. & Furthmüller, J. Efficiency of *ab-initio* total energy calculations for metals and semiconductors using a plane-wave basis set. *Comput. Mater. Sci.* **6**, 15–50 (1996).
66. Wang, V., Xu, N., Liu, J. C., Tang, G. & Geng, W. T. VASPKIT: a user-friendly interface facilitating high-throughput computing and analysis using VASP code. *Comput. Phys. Commun.* **267**, 108033 (2021).
67. Nosé, S. A unified formulation of the constant temperature molecular dynamics methods. *J. Chem. Phys.* **81**, 511–519 (1984).
68. Hoover, W. G. Canonical dynamics: equilibrium phase-space distributions. *Phys. Rev. A* **31**, 1695–1697 (1985).
69. Eckhoff, M. & Behler, J. From molecular fragments to the bulk: development of a neural network potential for MOF-5. *J. Chem. Theory Comput.* **15**, 3793–3809 (2019).
70. Eckhoff, M. & Behler, J. High-dimensional neural network potentials for magnetic systems using spin-dependent atom-centered symmetry functions. *npj Comput. Mater.* **7**, 170 (2021).
71. Artrith, N., Hiller, B. & Behler, J. Neural network potentials for metals and oxides – first applications to copper clusters at zinc oxide. *Phys. Status Solidi Basic Res.* **250**, 1191–1203 (2013).

72. Frenkel, D. & Smit, B. *Understanding Molecular Simulation* (Academic Press, 2002).
73. Henkelman, G., Uberuaga, B. P. & Jónsson, H. A climbing image nudged elastic band method for finding saddle points and minimum energy paths. *J. Chem. Phys.* **113**, 9901–9904 (2000).
74. Giorgino, T. Computing diffusion coefficients in macromolecular simulations: the Diffusion Coefficient Tool for VMD. *J. Open Source Softw.* **4**, 1698 (2019).
75. Du, Y. et al. Diffusion coefficients of some solutes in fcc and liquid Al: critical evaluation and correlation. *Mater. Sci. Eng. A* **363**, 140–151 (2003).
76. Álvarez-Moreno, M. et al. Managing the computational chemistry big data problem: the loChem-BD platform. *J. Chem. Inf. Model.* **55**, 95–103 (2015).

Acknowledgements

This work was funded by the European Union's Horizon Europe research and innovation programme under the Marie Skłodowska-Curie grant, agreement no. 101064867 (DESCRIPTOR project) and the Spanish Ministry of Science and Innovation (ref. no. PID2021-122516OB-I00, Severo Ochoa Center of Excellence CEX2019-000925-S). We thank the Barcelona Supercomputing Center (BSC-RES) for providing generous computational resources and technical support. We also thank N. Vendrell for her assistance in improving the writing language.

Author contributions

Z.L. and N.L. conceived this work and designed the simulations. Z.L. performed the calculations and the analysis. F.D. assisted with the analysis of coordination number and applied electric potential, and reviewed and edited the manuscript before submission. All authors contributed to writing the manuscript.

Competing interests

The authors declare no competing interests.

Additional information

Supplementary information The online version contains supplementary material available at <https://doi.org/10.1038/s41929-024-01132-5>.

Correspondence and requests for materials should be addressed to Zan Lian or Núria López.

Peer review information *Nature Catalysis* thanks Kari Laasonen and the other, anonymous, reviewer(s) for their contribution to the peer review of this work.

Reprints and permissions information is available at www.nature.com/reprints.

Publisher's note Springer Nature remains neutral with regard to jurisdictional claims in published maps and institutional affiliations.

Open Access This article is licensed under a Creative Commons Attribution 4.0 International License, which permits use, sharing, adaptation, distribution and reproduction in any medium or format, as long as you give appropriate credit to the original author(s) and the source, provide a link to the Creative Commons licence, and indicate if changes were made. The images or other third party material in this article are included in the article's Creative Commons licence, unless indicated otherwise in a credit line to the material. If material is not included in the article's Creative Commons licence and your intended use is not permitted by statutory regulation or exceeds the permitted use, you will need to obtain permission directly from the copyright holder. To view a copy of this licence, visit <http://creativecommons.org/licenses/by/4.0/>.

© The Author(s) 2024